Charged and strange hadron elliptic flow in Cu+Cu collisions at √sNN = 62.4 and 200 GeV

(STAR Collaboration) Abelev, B. I.; ...; Planinić, Mirko; ...; Poljak, Nikola; ...; Zoulkarneeva, Y.

Repository / Repozitorij:

Repository of the Faculty of Science - University of Zagreb

Charged and strange hadron elliptic flow in Cu + Cu collisions at $\sqrt{s_{NN}} = 62.4$ and 200 GeV

B. I. Abelev,[8] M. M. Aggarwal,[31] Z. Ahammed,[48] A. V. Alakhverdyants,[18] I. Alekseev,[16] B. D. Anderson,[19] D. Arkhipkin,[3]
G. S. Averichev,[18] J. Balewski,[23] L. S. Barnby,[2] S. Baumgart,[53] D. R. Beavis,[3] R. Bellwied,[51] M. J. Betancourt,[23] R. R. Betts,[8]
A. Bhasin,[17] A. K. Bhati,[31] H. Bichsel,[50] J. Bielcik,[10] J. Bielcikova,[11] B. Biritz,[6] L. C. Bland,[3] B. E. Bonner,[37] J. Bouchet,[19]
E. Braidot,[28] A. V. Brandin,[26] A. Bridgeman,[1] E. Bruna,[53] S. Bueltmann,[30] I. Bunzarov,[18] T. P. Burton,[3] X. Z. Cai,[41]
H. Caines,[53] M. Calderón de la Barca Sánchez,[5] O. Catu,[53] D. Cebra,[5] R. Cendejas,[6] M. C. Cervantes,[43] Z. Chajecki,[29]
P. Chaloupka,[11] S. Chattopadhyay,[48] H. F. Chen,[39] J. H. Chen,[41] J. Y. Chen,[52] J. Cheng,[45] M. Cherney,[9] A. Chikanian,[53]
K. E. Choi,[35] W. Christie,[3] P. Chung,[11] R. F. Clarke,[43] M. J. M. Codrington,[43] R. Corliss,[23] J. G. Cramer,[50] H. J. Crawford,[4]
D. Das,[5] S. Dash,[13] A. Davila Leyva,[44] L. C. De Silva,[51] R. R. Debbe,[3] T. G. Dedovich,[18] M. DePhillips,[3] A. A. Derevschikov,[33]
R. Derradi de Souza,[7] L. Didenko,[3] P. Djawotho,[43] S. M. Dogra,[17] X. Dong,[22] J. L. Drachenberg,[43] J. E. Draper,[5] J. C. Dunlop,[3]
M. R. Dutta Mazumdar,[48] L. G. Efimov,[18] E. Elhalhuli,[2] M. Elnimr,[51] J. Engelage,[4] G. Eppley,[37] B. Erazmus,[42] M. Estienne,[42]
L. Eun,[32] O. Evdokimov,[8] P. Fachini,[3] R. Fatemi,[20] J. Fedorisin,[18] R. G. Fersch,[20] P. Filip,[18] E. Finch,[53] V. Fine,[3] Y. Fisyak,[3]
C. A. Gagliardi,[43] D. R. Gangadharan,[6] M. S. Ganti,[48] E. J. Garcia-Solis,[8] A. Geromitsos,[42] F. Geurts,[37] V. Ghazikhanian,[6]
P. Ghosh,[48] Y. N. Gorbunov,[9] A. Gordon,[3] O. Grebenyuk,[22] D. Grosnick,[47] B. Grube,[35] S. M. Guertin,[6] A. Gupta,[17] N. Gupta,[17]
W. Guryn,[3] B. Haag,[5] A. Hamed,[43] L.-X. Han,[41] J. W. Harris,[53] J. P. Hays-Wehle,[23] M. Heinz,[53] S. Heppelmann,[32] A. Hirsch,[34]
E. Hjort,[22] A. M. Hoffman,[23] G. W. Hoffmann,[44] D. J. Hofman,[8] R. S. Hollis,[8] H. Z. Huang,[6] T. J. Humanic,[29] L. Huo,[43]
G. Igo,[6] A. Iordanova,[8] P. Jacobs,[22] W. W. Jacobs,[15] P. Jakl,[11] C. Jena,[13] F. Jin,[41] C. L. Jones,[23] P. G. Jones,[2] J. Joseph,[19]
E. G. Judd,[4] S. Kabana,[42] K. Kajimoto,[44] K. Kang,[45] J. Kapitan,[11] K. Kauder,[8] D. Keane,[19] A. Kechechyan,[18] D. Kettler,[50]
D. P. Kikola,[22] J. Kiryluk,[22] A. Kisiel,[49] S. R. Klein,[22] A. G. Knospe,[53] A. Kocoloski,[23] D. D. Koetke,[47] T. Kollegger,[12]
J. Konzer,[34] M. Kopytine,[19] I. Koralt,[30] L. Koroleva,[16] W. Korsch,[20] L. Kotchenda,[26] V. Kouchpil,[11] P. Kravtsov,[26] K. Krueger,[1]
M. Krus,[10] L. Kumar,[31] P. Kurnadi,[6] M. A. C. Lamont,[3] J. M. Landgraf,[3] S. LaPointe,[51] J. Lauret,[3] A. Lebedev,[3] R. Lednicky,[18]
C.-H. Lee,[35] J. H. Lee,[3] W. Leight,[23] M. J. LeVine,[3] C. Li,[39] L. Li,[44] N. Li,[52] W. Li,[41] X. Li,[40] X. Li,[34] Y. Li,[45] Z. Li,[52] G. Lin,[53]
S. J. Lindenbaum,[27,*] M. A. Lisa,[29] F. Liu,[52] H. Liu,[5] J. Liu,[37] T. Ljubicic,[3] W. J. Llope,[37] R. S. Longacre,[3] W. A. Love,[3]
Y. Lu,[39] G. L. Ma,[41] Y. G. Ma,[41] D. P. Mahapatra,[13] R. Majka,[53] O. I. Mall,[5] L. K. Mangotra,[17] R. Manweiler,[47] S. Margetis,[19]
C. Markert,[44] H. Masui,[22] H. S. Matis,[22] Yu. A. Matulenko,[33] D. McDonald,[37] T. S. McShane,[9] A. Meschanin,[33] R. Milner,[23]
N. G. Minaev,[33] S. Mioduszewski,[43] A. Mischke,[28] M. K. Mitrovski,[12] B. Mohanty,[48] M. M. Mondal,[48] B. Morozov,[16]
D. A. Morozov,[33] M. G. Munhoz,[38] B. K. Nandi,[14] C. Nattrass,[53] T. K. Nayak,[48] J. M. Nelson,[2] P. K. Netrakanti,[34] M. J. Ng,[4]
L. V. Nogach,[33] S. B. Nurushev,[33] G. Odyniec,[22] A. Ogawa,[3] H. Okada,[3] V. Okorokov,[26] D. Olson,[22] M. Pachr,[10] B. S. Page,[15]
S. K. Pal,[48] Y. Pandit,[19] Y. Panebratsev,[18] T. Pawlak,[49] T. Peitzmann,[28] V. Perevoztchikov,[3] C. Perkins,[4] W. Peryt,[49]
S. C. Phatak,[13] P. Pile,[3] M. Planinic,[54] M. A. Ploskon,[22] J. Pluta,[49] D. Plyku,[30] N. Poljak,[54] A. M. Poskanzer,[22]
B. V. K. S. Potukuchi,[17] C. B. Powell,[22] D. Prindle,[50] C. Pruneau,[51] N. K. Pruthi,[31] P. R. Pujahari,[14] J. Putschke,[53]
R. Raniwala,[36] S. Raniwala,[36] R. L. Ray,[44] R. Redwine,[23] R. Reed,[5] J. M. Rehberg,[12] H. G. Ritter,[22] J. B. Roberts,[37]
O. V. Rogachevskiy,[18] J. L. Romero,[5] A. Rose,[22] C. Roy,[42] L. Ruan,[3] R. Sahoo,[42] S. Sakai,[6] I. Sakrejda,[22] T. Sakuma,[23]
S. Salur,[5] J. Sandweiss,[53] E. Sangaline,[5] J. Schambach,[44] R. P. Scharenberg,[34] N. Schmitz,[24] T. R. Schuster,[12] J. Seele,[23]
J. Seger,[9] I. Selyuzhenkov,[15] P. Seyboth,[24] E. Shahaliev,[18] M. Shao,[39] M. Sharma,[51] S. S. Shi,[52,†] X. H. Shi,[41]
E. P. Sichtermann,[22] F. Simon,[24] R. N. Singaraju,[48] M. J. Skoby,[34] N. Smirnov,[53] P. Sorensen,[3] J. Sowinski,[15] H. M. Spinka,[1]
B. Srivastava,[34] T. D. S. Stanislaus,[47] D. Staszak,[6] J. R. Stevens,[15] R. Stock,[12] M. Strikhanov,[26] B. Stringfellow,[34]
A. A. P. Suaide,[38] M. C. Suarez,[8] N. L. Subba,[19] M. Sumbera,[11] X. M. Sun,[22] Y. Sun,[39] Z. Sun,[21] B. Surrow,[23] D. N. Svirida,[16]
T. J. M. Symons,[22] A. Szanto de Toledo,[38] J. Takahashi,[7] A. H. Tang,[3] Z. Tang,[39] L. H. Tarini,[51] T. Tarnowsky,[25] D. Thein,[44]
J. H. Thomas,[22] J. Tian,[41] A. R. Timmins,[51] S. Timoshenko,[26] D. Tlusty,[11] M. Tokarev,[18] V. N. Tram,[22] S. Trentalange,[6]
R. E. Tribble,[43] O. D. Tsai,[6] J. Ulery,[34] T. Ullrich,[3] D. G. Underwood,[1] G. Van Buren,[3] M. van Leeuwen,[28]
G. van Nieuwenhuizen,[23] J. A. Vanfossen Jr.,[19] R. Varma,[14] G. M. S. Vasconcelos,[7] A. N. Vasiliev,[33] F. Videbaek,[3]
Y. P. Viyogi,[48] S. Vokal,[18] S. A. Voloshin,[51] M. Wada,[44] M. Walker,[23] F. Wang,[34] G. Wang,[6] H. Wang,[25] J. S. Wang,[21]
Q. Wang,[34] X. L. Wang,[39] Y. Wang,[45] G. Webb,[20] J. C. Webb,[3] G. D. Westfall,[25] C. Whitten Jr.,[6] H. Wieman,[22] E. Wingfield,[44]
S. W. Wissink,[15] R. Witt,[46] Y. Wu,[52] W. Xie,[34] N. Xu,[22] Q. H. Xu,[40] W. Xu,[6] Y. Xu,[39] Z. Xu,[3] L. Xue,[41] Y. Yang,[21] P. Yepes,[37]
K. Yip,[3] I.-K. Yoo,[35] Q. Yue,[45] M. Zawisza,[49] H. Zbroszczyk,[49] W. Zhan,[21] S. Zhang,[41] W. M. Zhang,[19] X. P. Zhang,[22]
Y. Zhang,[22] Z. P. Zhang,[39] J. Zhao,[41] C. Zhong,[41] J. Zhou,[37] W. Zhou,[40] X. Zhu,[45] Y. H. Zhu,[41]
R. Zoulkarneev,[18] and Y. Zoulkarneeva[18]

(STAR Collaboration)

[1]*Argonne National Laboratory, Argonne, Illinois 60439, USA*
[2]*University of Birmingham, Birmingham, United Kingdom*
[3]*Brookhaven National Laboratory, Upton, New York 11973, USA*
[4]*University of California, Berkeley, California 94720, USA*
[5]*University of California, Davis, California 95616, USA*
[6]*University of California, Los Angeles, California 90095, USA*
[7]*Universidade Estadual de Campinas, Sao Paulo, Brazil*
[8]*University of Illinois at Chicago, Chicago, Illinois 60607, USA*

[9]*Creighton University, Omaha, Nebraska 68178, USA*
[10]*Czech Technical University in Prague, FNSPE, Prague, CZ-115 19, Czech Republic*
[11]*Nuclear Physics Institute AS CR, CZ-250 68 Řež/Prague, Czech Republic*
[12]*University of Frankfurt, Frankfurt, Germany*
[13]*Institute of Physics, Bhubaneswar 751005, India*
[14]*Indian Institute of Technology, Mumbai, India*
[15]*Indiana University, Bloomington, Indiana 47408, USA*
[16]*Alikhanov Institute for Theoretical and Experimental Physics, Moscow, Russia*
[17]*University of Jammu, Jammu 180001, India*
[18]*Joint Institute for Nuclear Research, Dubna, RU-141 980, Russia*
[19]*Kent State University, Kent, Ohio 44242, USA*
[20]*University of Kentucky, Lexington, Kentucky, 40506-0055, USA*
[21]*Institute of Modern Physics, Lanzhou, People's Republic of China*
[22]*Lawrence Berkeley National Laboratory, Berkeley, California 94720, USA*
[23]*Massachusetts Institute of Technology, Cambridge, Massachusetts 02139-4307, USA*
[24]*Max-Planck-Institut für Physik, Munich, Germany*
[25]*Michigan State University, East Lansing, Michigan 48824, USA*
[26]*Moscow Engineering Physics Institute, Moscow, Russia*
[27]*City College of New York, New York, New York 10031, USA*
[28]*NIKHEF and Utrecht University, Amsterdam, The Netherlands*
[29]*Ohio State University, Columbus, Ohio 43210, USA*
[30]*Old Dominion University, Norfolk, Virginia, 23529, USA*
[31]*Panjab University, Chandigarh 160014, India*
[32]*Pennsylvania State University, University Park, Pennsylvania 16802, USA*
[33]*Institute of High Energy Physics, Protvino, Russia*
[34]*Purdue University, West Lafayette, Indiana 47907, USA*
[35]*Pusan National University, Pusan, Republic of Korea*
[36]*University of Rajasthan, Jaipur 302004, India*
[37]*Rice University, Houston, Texas 77251, USA*
[38]*Universidade de Sao Paulo, Sao Paulo, Brazil*
[39]*University of Science & Technology of China, Hefei 230026, People's Republic of China*
[40]*Shandong University, Jinan, Shandong 250100, People's Republic of China*
[41]*Shanghai Institute of Applied Physics, Shanghai 201800, People's Republic of China*
[42]*SUBATECH, Nantes, France*
[43]*Texas A&M University, College Station, Texas 77843, USA*
[44]*University of Texas, Austin, Texas 78712, USA*
[45]*Tsinghua University, Beijing 100084, People's Republic of China*
[46]*United States Naval Academy, Annapolis, Maryland 21402, USA*
[47]*Valparaiso University, Valparaiso, Indiana 46383, USA*
[48]*Variable Energy Cyclotron Centre, Kolkata 700064, India*
[49]*Warsaw University of Technology, Warsaw, Poland*
[50]*University of Washington, Seattle, Washington 98195, USA*
[51]*Wayne State University, Detroit, Michigan 48201, USA*
[52]*Institute of Particle Physics, CCNU (HZNU), Wuhan 430079, People's Republic of China*
[53]*Yale University, New Haven, Connecticut 06520, USA*
[54]*University of Zagreb, Zagreb, HR-10002, Croatia*

We present the results of an elliptic flow, v_2, analysis of Cu + Cu collisions recorded with the solenoidal tracker detector (STAR) at the BNL Relativistic Heavy Ion Collider at $\sqrt{s_{NN}} = 62.4$ and 200 GeV. Elliptic flow as a function of transverse momentum, $v_2(p_T)$, is reported for different collision centralities for charged hadrons $h^{\pm}$ and strangeness-ontaining hadrons K_S^0, Λ, Ξ, and ϕ in the midrapidity region $|\eta| < 1.0$. Significant reduction in systematic uncertainty of the measurement due to nonflow effects has been achieved by correlating particles at midrapidity, $|\eta| < 1.0$, with those at forward rapidity, $2.5 < |\eta| < 4.0$. We also present azimuthal correlations in $p + p$ collisions at $\sqrt{s} = 200$ GeV to help in estimating nonflow effects. To study the system-size dependence of elliptic flow, we present a detailed comparison with previously published results from Au + Au collisions at $\sqrt{s_{NN}} = 200$ GeV. We observe that $v_2(p_T)$ of strange hadrons has similar scaling properties as were first observed in Au + Au collisions, that is, (i) at low transverse momenta, $p_T < 2$ GeV/c, v_2 scales with transverse kinetic

energy, $m_T - m$, and (ii) at intermediate p_T, $2 < p_T < 4 \, \mathrm{GeV}/c$, it scales with the number of constituent quarks, n_q. We have found that ideal hydrodynamic calculations fail to reproduce the centrality dependence of $v_2(p_T)$ for K_S^0 and Λ. Eccentricity scaled v_2 values, v_2/ε, are larger in more central collisions, suggesting stronger collective flow develops in more central collisions. The comparison with Au + Au collisions, which go further in density, shows that v_2/ε depends on the system size, that is, the number of participants N_{part}. This indicates that the ideal hydrodynamic limit is not reached in Cu + Cu collisions, presumably because the assumption of thermalization is not attained.

I. INTRODUCTION

At the early stages of relativistic heavy-ion collisions, a hot and dense, strongly interacting medium is created. The subsequent system evolution is determined by the nature of the medium. Experimentally, the dynamics of the system evolution has been studied by measuring the azimuthal anisotropy of the particle production relative to the reaction plane [1–3]. The centrality of the collision, defined by the transverse distance between the centers of the colliding nuclei called the impact parameter, results in an "almond-shaped" overlap region that is spatially azimuthal anisotropic. It is generally assumed that the initial spatial anisotropy in the system is converted into momentum-space anisotropy through rescatterings [4,5]. The elliptic flow, v_2, is the second harmonic coefficient of a Fourier expansion of the final momentum-space azimuthal anisotropy. Because of the self-quenching effect, it provides information about the dynamics at the early stage of the collisions [6–8]. Elliptic flow can provide information about the pressure gradients, the effective degrees of freedom, the degree of thermalization, and the equation of state of the matter created at the early stage. Thus, the centrality and system-size dependence of elliptic flow at different beam energies can be used to study the properties of the matter created in heavy-ion collisions [6].

Recently, two important insights have been obtained from the experimental results on v_2 as a function of transverse momentum, p_T, in Au + Au collisions at the BNL Relativistic Heavy Ion Collider (RHIC). First, in the low p_T region, $p_T < 2 \, \mathrm{GeV}/c$, the hadron mass hierarchy predicted by ideal hydrodynamic calculations is observed for identified hadrons π, K, K_S^0, p, Λ, and Ξ [9–13]. Even the ϕ and Ω, which are believed to have a reduced cross section for hadronic interactions [14–19], are consistent with the mass ordering [13,20,21]. Second, in the intermediate p_T region, $2 < p_T < 4 \, \mathrm{GeV}/c$, $v_2(p_T)$ follows a scaling depending on the number of constituent quarks within a given hadron, which can be explained via coalescence models [13,20,22]. Quark number scaling suggests that the system is in a partonic state and that the constituent quark degrees of freedom were relevant during the time v_2 was developed.

The STAR Collaboration's first published article showed that elliptic flow at RHIC is unexpectedly large [23], comparable to predictions of ideal hydrodynamic calculations [7,24–26]. This observation is among the evidence favoring

the picture of a nearly perfect liquid [27]. With the assumption of thermalization, ideal hydrodynamic calculations predict that the v_2 divided by spatial eccentricity, ε, does not depend on the collision centrality [28]. The spatial eccentricity is defined by [29]

$$\varepsilon = \frac{\langle y^2 - x^2 \rangle}{\langle y^2 + x^2 \rangle}, \tag{1}$$

where x and y are the spatial coordinates in the plane perpendicular to the collision axis. The angle brackets $\langle \ \rangle$ denote an average weighted by the initial density. However, recent RHIC v_2/ε data for charged hadrons $h^\pm$ and strangeness-containing hadrons K_S^0, ϕ, Λ, and Ξ show a trend to increase as a function of the particle density scaled by the system-size [30,31], lacking the saturation indicated by ideal hydrodynamic calculations [31]. This monotonic increase is a feature of a class of model descriptions that conform to the low-density limit [32]. Whether the thermalization and ideal hydrodynamic limit are reached or not at RHIC is not conclusive. A transport model suggested in Ref. [33] is constructed to link the low-density limit to the ideal hydrodynamic limit. In the microscopic transport picture, the ideal hydrodynamic limit is reached when the mean free path is very small or the cross section is very large. With this transport model approach, the degree of thermalization and the ideal hydrodynamic limit can be addressed [34].

The previous results mainly focus on the centrality dependence of charged hadrons and identified hadrons v_2 in Au + Au collisions. Because the conditions in Au + Au collisions might not hold in smaller systems and at lower beam energies, the system-size and beam-energy dependence of identified hadron elliptic flow will shed light on the properties of partonic collectivity and quark degrees of freedom. Further, the study of v_2 in collisions of nuclei smaller than Au + Au will allow us to test the early thermalization hypothesis in Au + Au collisions. To date, there are only a few studies of an identified hadron v_2 in Cu + Cu collisions. In this article, we present the results on the azimuthal anisotropy parameter $v_2(p_T)$ of $h^\pm$, K_S^0, Λ, Ξ, and ϕ from $\sqrt{s_{NN}} = 62.4$ and 200 GeV Cu + Cu collisions. As a function of collision centrality, the scaling properties of v_2 with the transverse kinetic energy $m_T - m$ and the number of constituent quarks n_q are reported. In the quantity $m_T = \sqrt{p_T^2 + m^2}$, m denotes the rest mass of a given hadron. We also discuss system-size dependence in this article.

The rest of the article is organized in the following way: Section II summarizes the analysis details including data and centrality selections, particle identification and flow methods used for charged hadrons and identified hadrons.

_____

*Deceased.

†Corresponding author: sss@iopp.ccnu.edu.cn

In the following, we use $h^{\pm}$, Λ, and Ξ to denote charged hadron, $\Lambda + \overline{\Lambda}$, and $\Xi^- + \overline{\Xi}^+$, respectively. In Sec. III, we present measurements of v_2 for $h^{\pm}$ in Cu + Cu collisions from different analysis methods. Differences in v_2 are used to estimate the systematic error. Section IV presents the results and physics discussion of the scaling properties and system-size dependence along with ideal hydrodynamic calculations. Last, a summary is presented in Sec. V.

II. EXPERIMENTS AND ANALYSIS

A. Experiments and data sets

For this article, our data were collected from $\sqrt{s_{NN}} = 62.4$ and 200 GeV Cu + Cu collisions with the solenoidal tracker at RHIC (STAR) detector during the fifth RHIC run in 2005. In addition data from $\sqrt{s_{NN}} = 200$ GeV $p + p$ collisions in 2005 were used in the analysis of nonflow contributions. STAR's main time projection chamber (TPC) [35] and two forward time projection chambers (FTPCs) [36] were used for particle tracking in the central region ($|\eta| < 1.0$) and forward regions ($2.5 < |\eta| < 4.0$), respectively. Both the TPC and FTPCs provide azimuthal acceptance over 2π. Only those events that have the primary vertex position along the longitudinal beam direction (V_z) within 30 cm of the nominal collision point are selected for the analysis. This is done in order to have a more uniform detector performance within $|\eta| < 1.0$. The centrality definition, which is based on the raw charged particle TPC multiplicity with $|\eta| < 0.5$, is the same as that used previously [37]. After quality cuts, the number of the 60% most central events is about 24 million for 200 GeV Cu + Cu collisions and 10 million for 62.4 GeV Cu + Cu collisions. The results from more peripheral collisions are not presented because of trigger inefficiencies at low multiplicity.

The centrality was defined using the number of charged tracks with quality cuts similar to those in Ref. [31]. The 60% most central events for v_2 analysis of $h^{\pm}$ were divided into six centrality bins, each spanning an interval of 10% of the geometric cross section. For v_2 analysis of K_S^0 and Λ, centrality bins of 0%–20% and 20%–60% were used. To reduce the multiplicity fluctuations in wide centrality bins, we calculated v_2 in the 10% wide bins, then combined them using particle yield as the weight.

To select good tracks from primary collisions, charged particle tracks coming from the collision that transversed the TPC or FTPCs were selected by requiring the distance of closest approach to the primary vertex be less than 3 cm. Tracks used for K_S^0, Λ, and Ξ reconstruction were not subject to this cut. We required that the TPC and FTPCs had a number of hits used for reconstruction of the tracks of the particles >15 and >5, respectively. For the TPC and FTPCs the ratio of the number of fit hits to maximum possible hits was >0.52. An additional transverse momentum cut ($0.15 < p_T < 2$ GeV/c) was applied to the charged tracks for the event plane determination.

B. Particle identification

We utilized the topology of decay as measured with the TPC inside the magnetic field to identify K_S^0, ϕ, Λ ($\overline{\Lambda}$), and Ξ^- ($\overline{\Xi}^+$). We used the following decay channels: $K_S^0 \rightarrow \pi^+ + \pi^-$, $\phi \rightarrow K^+ + K^-$, $\Lambda \rightarrow p + \pi^-$ ($\overline{\Lambda} \rightarrow \overline{p} + \pi^+$), and $\Xi^- \rightarrow \Lambda + \pi^-$ ($\overline{\Xi}^+ \rightarrow \overline{\Lambda} + \pi^+$). Similar to the previous analysis in Ref. [31], topological and kinematic cuts were applied to reduce the combinatorial backgrounds. Figure 1 shows the invariant mass distributions for (a) K_S^0, (b) ϕ, (c) Λ, and (d) Ξ for selected p_T bins in $\sqrt{s_{NN}} = 200$ GeV Cu + Cu 60% most central collisions. The cuts used for Cu + Cu collisions are similar to those for Au + Au collisions in Ref. [31]. The combinatorial backgrounds were estimated from the fourth-order polynomial fits for K_S^0 and Λ [31]. The invariant mass distribution for ϕ is after subtraction of combinatorial background estimated using event mixing [38]; the remaining combinatorial backgrounds were estimated by a first-order polynomial fit [20]. For Ξ, the background was estimated by rotating the transverse momentum of the daughter Λ by 180°. This operation breaks the correlation between the Λ and the other daughter particle. The resulting invariant mass distributions provide a good approximation of the true background distribution. The detailed description of the method can be found in Refs. [12,13].
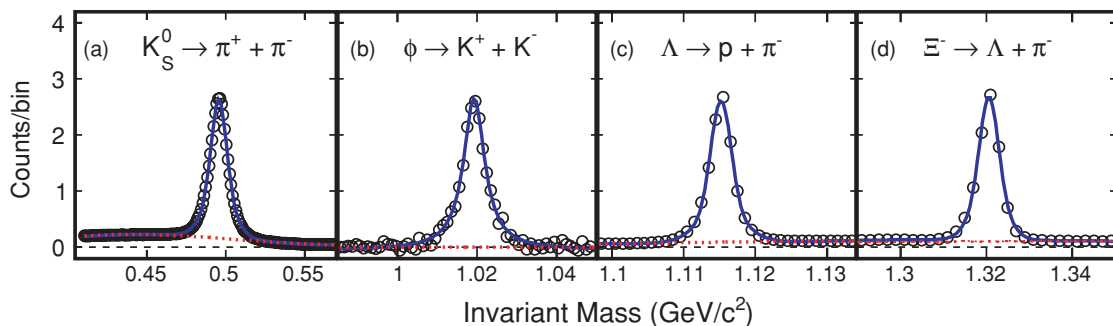

FIG. 1. (Color online) Invariant mass distributions for (a) K_S^0 ($1.2 < p_T < 1.4$ GeV/c), (b) ϕ ($1.0 < p_T < 2.0$ GeV/c), (c) Λ ($1.4 < p_T < 1.6$ GeV/c), and (d) Ξ ($1.25 < p_T < 1.75$ GeV/c) in $\sqrt{s_{NN}} = 200$ GeV Cu + Cu 60% most central collisions. The solid curves represent the fits to the invariant mass distributions: Gaussians plus fourth-order polynomials for K_S^0, Λ, and Ξ, and Breit-Wigner plus a linear function for ϕ. The dotted curves are the estimated backgrounds: the fourth-order polynomials for K_S^0 and Λ, a linear function for ϕ, and a rotation method described in the text for Ξ. For clarity, the invariant mass distributions for K_S^0, Λ, ϕ, and Ξ are scaled by 1/50 000, 1/130 000, 1/5000 and 1/8000, respectively. The error bars are shown only for the statistical uncertainties.

C. Flow methods

Anisotropic flow, which is an anisotropy in the particle production relative to the reaction plane, results in correlations among particles and can be studied by the analysis of these correlations. At the same time these correlations are affected by other effects that are not related to the orientation of the reaction plane. Such are commonly referred to as nonflow, and are due, for example, to resonance decays and jet production. Different methods used to measure anisotropic flow are affected by nonflow effects in different ways and are used in this analysis to evaluate the systematic uncertainty of the measurements.

1. Event plane method with TPC event plane

The event plane method [2] uses the anisotropic flow itself to determine the event plane (the estimated reaction plane), which can be done for each harmonic. The second-harmonic flow vector, Q_2, of the event is constructed using the TPC tracks i in the event with their azimuthal angle, ϕ_i, according to Eqs. (2) and (3). To maximize the resolution of the flow effect, the weights w_i are set equal to p_T up to 2 GeV/c:

$$Q_2 \cos(2\Psi_2) = Q_{2x} = \sum_i w_i \cos(2\phi_i), \qquad (2)$$

$$Q_2 \sin(2\Psi_2) = Q_{2y} = \sum_i w_i \sin(2\phi_i) \qquad (3)$$

Elliptic flow is first calculated with respect to the event plane angle Ψ_2 as shown in Eq. (4), which is called the observed v_2. The angle brackets indicate an average over all particles in all events. However, tracks used for the v_2 calculation are excluded from the calculation of the flow vector to remove autocorrelation effects. Then the observed v_2 is corrected by the event plane resolution [the denominator in Eq. (5)] to obtain v_2 relative to the event plane:

$$v_2^{\text{obs}} = \langle \cos[2(\phi - \Psi_2)] \rangle, \qquad (4)$$

$$v_2 = \frac{v_2^{\text{obs}}}{\langle \cos[2(\Psi_2 - \Psi_r)] \rangle}. \qquad (5)$$

The results are denoted as $v_2\{\text{TPC}\}$ in the following.

Because the reaction plane is unknown, the denominator in Eq. (5) is still not calculable. As shown in Eq. (6), we estimate the event plane resolution by the correlations between the azimuthal angles of two subset groups of tracks, called subevents A and B. In this analysis, we use two random subevents with equal numbers of particles. In Eq. (6), C is a constant calculated from the known multiplicity dependence of the resolution [2]:

$$\langle \cos[2(\Psi_2 - \Psi_r)] \rangle = C \sqrt{\langle \cos\left[2\left(\Psi_2^A - \Psi_2^B\right)\right] \rangle}. \qquad (6)$$

In the case of low resolution ($\leqslant 0.2$), such as for the FTPC event plane, C approaches $\sqrt{2}$.

The reaction plane azimuthal distribution should be isotropic in the laboratory frame. Thus, the event plane azimuthal distribution must be flat if the detectors have ideal acceptance. Because the detectors usually have nonuniform acceptance, a procedure for flattening the event plane distri-

bution is necessary. For the event plane reconstructed from TPC tracks, the ϕ weight method is an effective way to flatten the distribution. The ϕ weights are generated by inverting the ϕ distributions of detected tracks for a large event sample. The detector acceptance bias is removed by applying the ϕ weight at the ϕ of each track to that track. The ϕ weights are folded into the weight w_i in Eqs. (2) and (3). Independent corrections were applied to each centrality selection in 10% increments and in two bins in the primary vertex position along the longitudinal beam direction (V_z). The corrections were done on a run-by-run basis (around 50k events).

2. Event plane method with FTPC event plane

The η gap between two FTPCs sitting at two sides of the collision in the forward regions can be used to reduce nonflow effects due to short-range correlations. The basic procedures are similar to those for the event plane method with the TPC event plane. There are three steps: estimate the event plane with FTPC tracks, calculate v_2 with respect to the event plane, and obtain the real v_2 by correction to the real reaction plane. Equations (2)–(6) can be applied, except that (i) the sums in Eqs. (2) and (3) go over FTPC tracks instead of TPC tracks and (ii) two subset groups of tracks are classified according to the sign of η. The tracks with $-4 < \eta < -2.5$ and $2.5 < \eta < 4$ are called east subevent and west subevent, respectively. Hence, the resolution in Eq. (6) is calculated by the correlation between the azimuthal angles Ψ_2^{east} and Ψ_2^{west}. The average in Eq. (4) runs over the TPC tracks as before. The result of this procedure is denoted as $v_2\{\text{FTPC}\}$.

Because of the serious loss of acceptance for FTPCs due to partially nonfunctioning readout electronics, the number of tracks detected by the best sector is about 6 times greater than that for the worst one. The result is that the ϕ weight method is not enough to generate a flat event plane distribution. Thus, further small corrections are applied after ϕ weight corrections using the shift method [39]. Equation (7) shows the formula for the shift correction. The averages in Eq. (7) are taken from a large sample of events. In this analysis, the correction is done up to the 20th harmonic. This was done to make the χ^2 divided by the number of degrees of freedom of a flat fit to the event plane azimuthal angle distribution to be less than 1. The distributions of Ψ_2^{east} and Ψ_2^{west} are separately flattened and then the full-event event plane distribution is flattened. Accordingly, the observed v_2 and resolution are calculated using the shifted (sub)event plane azimuthal angles.

$$\Psi' = \Psi + \sum_n \frac{1}{n}[-\langle \sin(2n\Psi) \rangle \cos(2n\Psi)$$
$$+ \langle \cos(2n\Psi) \rangle \sin(2n\Psi)]. \qquad (7)$$

3. Scalar product method

The scalar product method [30,40] is similar to the event plane method and gives v_2 as

$$v_2(p_T) = \frac{\langle Q_2 u_{2,i}^*(p_T) \rangle}{2\sqrt{\langle Q_2^A Q_2^{B*} \rangle}}, \qquad (8)$$

where $u_{2,i} = \cos(2\phi_i) + i\sin(2\phi_i)$ is a unit vector of the ith particle and $Q_2 = \sum_k u_{2,k}$ is the flow vector with the sum running over all other particles k in the event. The superscript $*$ denotes the complex conjugate of a complex number. A and B denote the two subevents. In the case that Q_2 is normalized to a unit vector, Eq. (8) reduces to the event plane method. In the scalar product method, one can use a different (recentering) technique [41] to correct for detector effects, which presents an alternative to the weighting and shifting procedures described in Secs. II C 1 and II C 2 above. The scalar product method is applied to the v_2 measurement of charged hadrons.

D. v_2 versus $m_{\rm inv}$ method

For v_2 of the identified particles K_S^0, ϕ, Λ, and Ξ, the v_2 versus $m_{\rm inv}$ method is used [31,42]. Because v_2 is additive, one can write the total $v_2^{\rm Sig+Bg}$ as a sum of signal and background contributions weighted by their relative yields:

$$
\begin{aligned}
&v_2^{\rm Sig+Bg}(m_{\rm inv}) \\
&= v_2^{\rm Sig}\frac{\rm Sig}{\rm Sig+Bg}(m_{\rm inv}) + v_2^{\rm Bg}(m_{\rm inv})\frac{\rm Bg}{\rm Sig+Bg}(m_{\rm inv}).
\end{aligned} \quad (9)
$$

This method involves the calculation of $v_2^{\rm Sig+Bg}$ as a function of $m_{\rm inv}$ and then fitting the distribution using Eq. (9) with measured relative yields and parametrizations of $v_2^{\rm Sig}$ and $v_2^{\rm Bg}$. The $({\rm Bg/Sig+Bg})(m_{\rm inv})$ distribution is the Bg divided by $({\rm Sig+Bg})$. The $({\rm Sig/Sig+Bg})(m_{\rm inv})$ distribution is simply calculated by $1 - ({\rm Bg/Sig+Bg})(m_{\rm inv})$. The term $v_2^{\rm Bg}$ is parametrized as a linear function to take care of the nonconstant $v_2^{\rm Bg}$ value as a function of $m_{\rm inv}$. The fit result $v_2^{\rm Sig}$ is the final observed v_2. Why this method works well for measuring signal v_2 is explained as follows: a set of data points is used in the fit over a wide $m_{\rm inv}$ region for Sig and Bg. Data points far from the mass peak constrain $v_2^{\rm Bg}(m_{\rm inv})$, because pure Bg is expected in this region. Under the peak, $v_2^{\rm Sig+Bg}(m_{\rm inv})$ is dominated by the Sig distribution. Finally, the v_2 signal is extracted by the fitting method shown in Eq. (9).

Note that the subtraction procedure used to extract the v_2 signal for a given identified particle is independent of the flow correlations. The v_2 distributions of the overall signal and background are evaluated by one of the flow analysis methods discussed in Secs. II C 1–II C 3. In this article, the event plane method with the FTPC event plane is applied for K_S^0, ϕ, Λ, and Ξ.

E. Nonflow contribution for various methods

The method of determining v_2 using cumulants of various orders has been shown to eliminate nonflow correlations. However, the method is useful only for large values of flow and multiplicity. For the relatively low values of flow and multiplicity seen in Cu + Cu collisions, the nonflow correlations have been estimated, as described subsequently.

The event plane method with the TPC event plane is sensitive to nonflow effects. Particles of interest tend to correlate with particles used in the flow vector calculation

because of short-range nonflow correlations. Also, particles of two random subevents tend to have those correlations. Thus, nonflow exists in both the observed v_2 [Eq. (4)] and the resolution [Eq. (6)]. To reduce nonflow effects due to short-range correlations, we take advantage of the large η gap between the two FTPCs sitting at the two sides of the collision in the forward regions. Nonflow is reduced by the η gap between the TPC and FTPCs, but this may not be large enough to remove all nonflow correlations. Thus, we investigate these effects by comparing the azimuthal correlations measured in Cu + Cu to those in $p + p$ collisions, where all correlations are assumed to be of nonflow origin [43]. Taking into account the nonflow contribution, the numerator of Eq. (8) can be written as follows [30,43]:

$$
\begin{aligned}
\langle Q_2 u_{2,i}^*(p_T)\rangle &= \left\langle \sum_k \cos[2(\phi_{p_T} - \phi_k)]\right\rangle \\
&= M v_2(p_T)\overline{v_2} + \text{nonflow}, \quad (10)
\end{aligned}
$$

where ϕ_{p_T} is the azimuthal angle of particles from a given p_T bin [$u_{2,i}^*$ in Eq. (8)] and the sum goes over all tracks k in an event used to determine the flow vector [Q_2 in Eq. (8)]. The angled brackets denote averaging over the events. The first term in the right-hand side of Eq. (10) represents the contribution from elliptic flow. $v_2(p_T)$ is the value of elliptic flow at a given p_T. $\overline{v_2}$ is the elliptic flow on average for all particles used in the sum of Eq. (10). The multiplicity of particles contributing to the sum is denoted by M. All other correlations subject to nonflow go to the second term in the right-hand side of Eq. (10). It is assumed that the quantity $\langle Q_2 u_{2,i}^*(p_T)\rangle$ in $p + p$ collisions can be used to estimate the nonflow in AA collisions [40,43]:

$$
M v_2(p_T)\overline{v_2} = \langle Q_2 u_{2,i}^*(p_T)\rangle_{AA} - \langle Q_2 u_{2,i}^*(p_T)\rangle_{pp}. \quad (11)
$$

Dividing both sides by $2\sqrt{\langle Q_2^A Q_2^{B*}\rangle_{AA}}$ as in Eq. (8) gives

$$
v_2\{AA-pp\}(p_T) = \frac{\langle Q_2 u_{2,i}^*(p_T)\rangle_{AA} - \langle Q_2 u_{2,i}^*(p_T)\rangle_{pp}}{2\sqrt{\langle Q_2^A Q_2^{B*}\rangle_{AA}}}
$$

$$
(12)
$$

because $2\sqrt{\langle Q_2^A Q_2^{B*}\rangle_{AA}} = 2\sqrt{(M/2)\overline{v_2}(M/2)\overline{v_2}} = M\overline{v_2}$.

Comparing $p + p$ and AA collisions, one might expect some changes in particle correlations: there could be an increase in correlations due to a possible increase of jet multiplicities in AA collisions or, conversely, some decrease due to the suppression of high p_T back-to-back correlations [44]. Hoever, AA collisions exhibit long η range correlations (the "ridge") [45,46], which are not seen in $p + p$ collisions and the origin of which is under investigation [47]. Thus it is difficult to make an accurate estimate of nonflow contributions. The fact that at high p_T ($p_T > 5$ GeV/c) the $p + p$ results are very close to central Au + Au [40,43] suggests that the uncertainties are relatively small. In the following we estimate the systematic uncertainties arising from nonflow contributions. We use $v_2\{AA-pp, {\rm TPC}\}$ and $v_2\{AA-pp, {\rm FTPC}\}$ to denote $v_2\{AA-pp\}$ calculated with TPC and FTPC flow vectors, respectively.
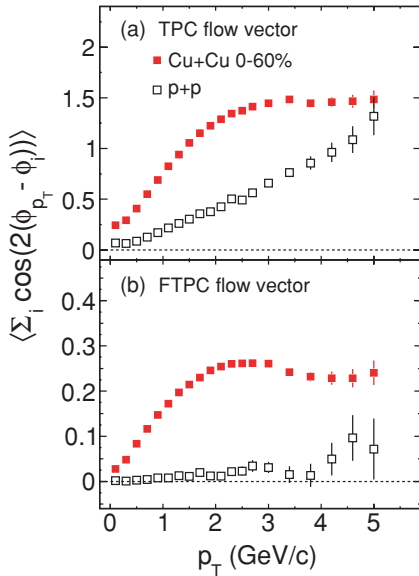
FIG. 2. (Color online) Charged hadron azimuthal correlations as a function of p_T in $\sqrt{s_{NN}} = 200$ GeV 60% most central Cu + Cu collisions (solid squares) compared to those from $\sqrt{s_{NN}} = 200$ GeV $p + p$ collisions (open squares). Flow vector calculated from (a) TPC tracks and (b) FTPC tracks. The error bars are shown only for the statistical uncertainties.

III. SYSTEMATIC UNCERTAINTIES

Nonflow is one of the largest uncertainties in elliptic flow measurements. As we mentioned in Sec. II C, this effect can be investigated by comparing the azimuthal correlations measured in Cu + Cu collisions to those in $p + p$ collisions. The event average of the sum of the correlations is given by Eq. (10).

Figure 2 shows the azimuthal correlation, Eq. (10), as a function of p_T for the 0%–60% centrality range in Cu + Cu collisions at $\sqrt{s_{NN}} = 200$ GeV, compared to $p + p$ collisions. As we can see, the azimuthal correlations in Cu + Cu collisions, shown as solid squares, increase with p_T and then saturate above 2GeV/c while those in $p + p$ collisions, shown as open squares, monotonically increase with p_T in the case of the TPC flow vector. With the flow vector determined from FTPC tracks the azimuthal correlations around midrapidity in $p + p$ collisions are small when p_T is less than 4GeV/c. This means that one strongly reduces the nonflow effects with the FTPC flow vector relative to the one seen with the TPC flow vector.

To illustrate the sensitivity to nonflow for the various flow analysis methods, we first analyzed $h^{\pm}$ elliptic flow in the 60% most central Cu + Cu collisions at $\sqrt{s_{NN}} = 200$ GeV. As shown in Fig. 3(a), the fact that $v_2\{\text{TPC}\}$ is significantly larger than $v_2\{\text{FTPC}\}$ indicates a larger nonflow effect in $v_2\{\text{TPC}\}$. With the large η gap between west and east FTPCs, nonflow effects due to the short-range correlations are reduced in $v_2\{\text{FTPC}\}$. $v_2\{\text{FTPC}\}$ saturates at $p_T \sim 2.5$ GeV/c and then falls off slightly up to $p_T \sim 4$ GeV/c. To estimate the remaining nonflow effects in $v_2\{\text{FTPC}\}$, we subtract the azimuthal correlations of $p + p$ collisions from those in Cu + Cu collisions according to Eq. (12). In Fig. 3(a),
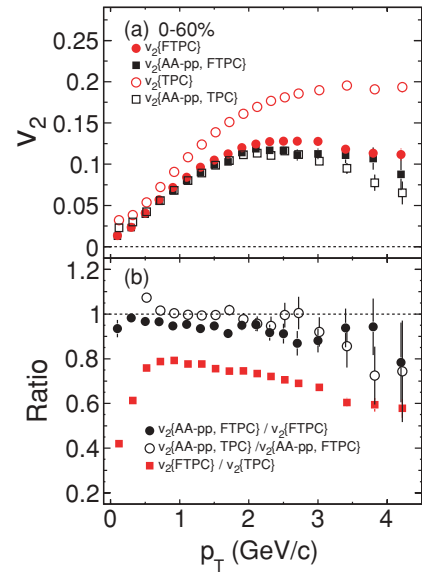

FIG. 3. (Color online) (a) Charged hadron $v_2(p_T)$ in $\sqrt{s_{NN}} = 200$ GeV 0%–60% Cu + Cu collisions. Open circles, solid circles, open squares, and solid squares represent the results of v_2 as function of p_T measured by the TPC flow vector ($v_2\{\text{TPC}\}$), the FTPC flow vector ($v_2\{\text{FTPC}\}$), and the TPC and FTPC flow vectors with subtracting the azimuthal correlations in $p + p$ collisions ($v_2\{AA - pp, \text{TPC}\}$, $v_2\{AA - pp, \text{FTPC}\}$). (b) The ratio of the results for the various methods described in panel (a). The error bars are shown only for the statistical uncertainties.

$v_2\{AA - pp, \text{FTPC}\}$ is close to $v_2\{\text{FTPC}\}$ in the region $p_T < 4$ GeV/c. To quantitatively illustrate nonflow systematic uncertainties, Fig. 3(b) shows the ratios of $v_2\{AA - pp, \text{FTPC}\}$ to $v_2\{\text{FTPC}\}$, $v_2\{AA - pp, \text{TPC}\}$ to $v_2\{AA - pp, \text{FTPC}\}$, and $v_2\{\text{FTPC}\}$ to $v_2\{\text{TPC}\}$ as a function of p_T. $v_2\{\text{FTPC}\}/v_2\{\text{TPC}\}$ shows that nonflow in $v_2\{\text{TPC}\}$ increases from 20% at $p_T \sim 0.8$ GeV/c to 40% at $p_T \sim 3.5$ GeV/c. Based on the comparison between $v_2\{AA - pp, \text{FTPC}\}$ and $v_2\{\text{FTPC}\}$, the residual nonflow in $v_2\{\text{FTPC}\}$ is less than 10% below $p_T \sim 4$ GeV/c. We also checked the $v_2\{AA - pp\}$ calculated with the TPC flow vector. Beyond $p_T \sim 3$ GeV/c, $v_2\{AA - pp, \text{TPC}\}$ seems systematically lower, but within errors it is similar to $v_2\{AA - pp, \text{FTPC}\}$. This shows that most of the nonflow is eliminated by subtracting the azimuthal correlation in $p + p$ collisions, validating our earlier assumption.

To illustrate the centrality dependence of the systematic uncertainties, Fig. 4 shows $v_2\{\text{FTPC}\}$ and $v_2\{AA - pp, \text{FTPC}\}$ as a function of p_T for six centrality bins. Ratios of $v_2\{AA - pp, \text{FTPC}\}$ to $v_2\{\text{FTPC}\}$ for each centrality bin are shown in Fig. 5 from (a) the most peripheral bin 50%–60% to (f) the most central bin 0%–10%. For each centrality bin, the ratio falls off slightly as p_T increases. For the two peripheral bins 50%–60% and 40%–50%, the ratios drop faster than in the other bins, indicating larger nonflow contributions in $v_2\{\text{FTPC}\}(p_T)$ in peripheral Cu + Cu collisions. Figure 6 shows charged hadron v_2 integrated over p_T ($0.15 < p_T < 4$ GeV/c) and η ($|\eta| < 1.0$) vs centrality for the various methods. It is clear that $v_2\{\text{TPC}\}$ is much higher than for the other methods, especially for the peripheral collisions.
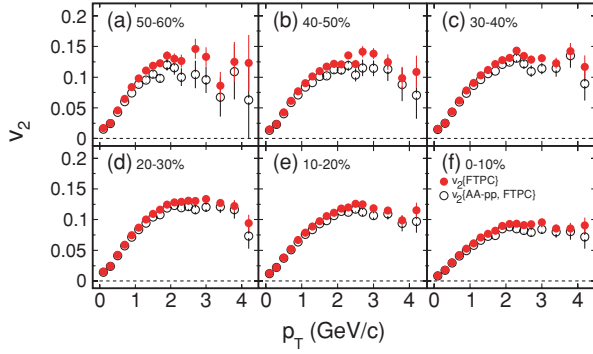
FIG. 4. (Color online) Charged hadron $v_2\{FTPC\}$ (solid circles) and $v_2\{AA - pp, FTPC\}$ (open circles) as a function of p_T in $\sqrt{s_{NN}} = 200$ GeV Cu + Cu collisions for centrality bins: (a) 50%–60%, (b) 40%–50%, (c) 30%-40%, (d) 20%–30%, (e) 10%–20%, and (f) 0%–10%. The percentages refer to fractions of most central events. The error bars are shown only for the statistical uncertainties.

To summarize the nonflow systematics we employed the scalar product method with TPC and FTPC flow vectors for $h^\pm$ in Cu + Cu collisions at $\sqrt{s_{NN}} = 200$ GeV. The results for the 60% most central events are shown in Fig. 3. $v_2\{TPC\}$ has large nonflow contributions while $v_2\{FTPC\}$ eliminates most of the nonflow. In what follows, we report our results in terms of $v_2\{FTPC\}$. For simplicity v_2 denotes $v_2\{FTPC\}$ except when the flow method is explicitly specified. With the assumption of pure nonflow effects in $p + p$ collisions, we use $v_2\{AA - pp, FTPC\}$ to estimate nonflow systematic errors in $v_2\{FTPC\}$. Ratios of $v_2\{AA - pp, FTPC\}$ to $v_2\{FTPC\}$ are shown for the 60% most central events in Fig. 3(b) and six centrality bins in Fig. 5. The ratios show that nonflow effects increase with p_T for all centrality bins and nonflow effects are larger in more peripheral bins. To estimate the nonflow systematic error in $v_2\{FTPC\}$, we fitted a constant to the ratio $v_2\{AA - pp, FTPC\}/v_2\{FTPC\}$ in the p_T range (0, 4 GeV). We take the numerical value of this constant as the estimate of the systematic uncertainty. The resulting nonflow systematic
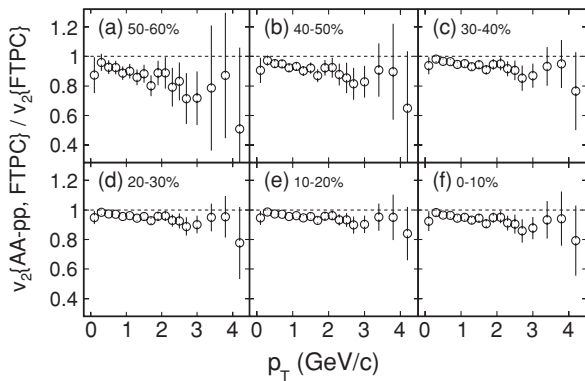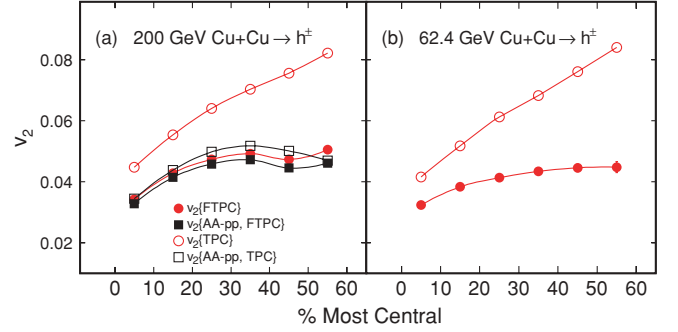

FIG. 5. Ratios of $v_2\{AA - pp, FTPC\}/v_2\{FTPC\}$ for charged hadrons as a function of p_T in $\sqrt{s_{NN}} = 200$ GeV Cu + Cu collisions for centrality bins: (a) 50%–60%, (b) 40%–50%, (c) 30%–40%, (d) 20%–30%, (e) 10%–20%, and (f) 0%–10%. The percentages refer to fractions of most central events.

FIG. 6. (Color online) Charged hadron v_2 integrated over p_T and η vs centrality for the various methods described in the text in $\sqrt{s_{NN}} = 200$ and 62.4 GeV Cu + Cu collisions. The error bars are shown only for the statistical uncertainties.

error is minus 5% for 0%–10%, 10%–20%, 20%–30%, and 30%–40% collisions and minus 10% for 40%–50% and 50%–60% collisions. Although for v_2 of K_S^0, ϕ, Λ, and Ξ the nonflow effects may be different, because we don't have enough statistics to repeat the analysis we simply assume a similar magnitude for the nonflow systematic error.

The other systematic uncertainties in the v_2 analysis procedure are studied as follows. We estimate the systematic errors from the shifting method for the FTPC event plane by comparing v_2 using different maximum harmonics in Eq. (7) and find the systematic errors are less than 1%. The systematic errors in K_S^0 and Λ v_2 resulting from the background uncertainty and topological cut criteria are estimated using the event plane method. The uncertainty due to the background subtraction is estimated as the relative differences in v_2 from fitting the background using second- and fourth-order polynomials. The systematic uncertainty is also estimated by varying the cut parameters. The systematic errors for K_S^0 and Λ from the background uncertainty and the cut criteria are summarized in Table I. From Ref. [31], the estimated systematic uncertainty of Λ from feed-down is less than 2%.

IV. RESULTS AND DISCUSSION

A. Charged hadrons

Flow results for charged hadrons were determined using the scalar product method Eq. (8) with the flow vector derived from the FTPC tracks. A comparison to $v_2\{AA - pp, FTPC\}$ Eq. (12) was used to estimate the systematic error. Figure 7 shows $v_2(p_T)$ of $h^\pm$ for six centrality bins from Cu + Cu

TABLE I. Summary of systematic errors of v_2 due to the reconstruction procedure of strange hadrons in Cu + Cu collisions at $\sqrt{s_{NN}} = 200$ GeV.

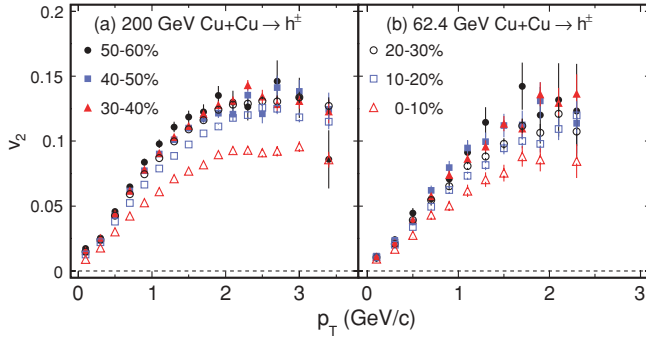| Centrality	K_S^0		Λ	
	Background	Cut criteria	Background	Cut criteria
0%–60%	1%	2%	1%	2%
0%–20%	1%	2%	1%	4%
20%–60%	4%	1%	5%	1%

FIG. 7. (Color online) Charged hadron v_2 as a function of p_T for 50%–60% (solid circles), 40%–50% (solid squares), 30%–40% (solid triangles), 20%–30% (open circles), 10%–20% (open squares), and 0%–10% (open triangles) in $\sqrt{s_{NN}} = 200$ GeV and 62.4 GeV Cu + Cu collisions. The error bars are shown only for the statistical uncertainties.

FIG. 8. (Color online) (a) Charged hadron v_2 as a function of p_T in Cu + Cu collisions. The results from $\sqrt{s_{NN}} = 200$ GeV and 62.4 GeV are presented by open symbols and solid symbols, respectively. (b) Ratios of the $v_2(p_T)$ from $\sqrt{s_{NN}} = 62.4$ GeV to 200 GeV. The error bars are shown only for the statistical uncertainties.

collisions at $\sqrt{s_{NN}} = 200$ and 62.4 GeV. For a given centrality bin, $v_2(p_T)$ initially increases with p_T. At higher p_T($p_T > 2$ GeV/c), v_2 appears to saturate or decrease. $v_2(p_T)$ in more peripheral collisions increases faster and reaches higher values as expected for the larger eccentricity.

At low p_T, the increase of $v_2(p_T)$ with p_T is consistent with predictions from ideal hydrodynamic calculations, which will be shown in Fig. 9 for identified particles. The model predicts that v_2 continues increasing beyond $p_T \sim 2$ GeV/c. The observed saturation or decrease of $v_2(p_T)$ indicates that the model is not valid in this region. One expects that the model should be valid up to higher p_T in a system with larger densities and larger volumes. This was observed in 200 GeV Au + Au collisions [48] where $v_2(p_T)$ of $h^{\pm}$ saturated at higher p_T in more central collisions. However, we do not observe the strong centrality dependence of saturation p_T for 200 GeV Cu + Cu collisions.
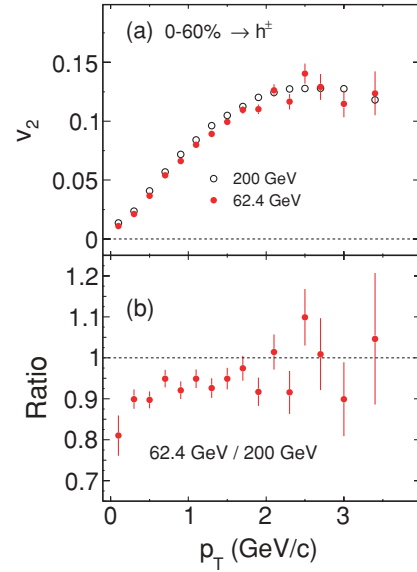
Figure 8 shows the comparison of v_2 for $h^{\pm}$ from $\sqrt{s_{NN}} = 62.4$ and 200 GeV Cu + Cu collisions. The p_T dependence of v_2 at the two energies is similar.

B. Identified hadrons

The event plane method Eqs. (2)–(5) with the event plane determined from the FTPC tracks was applied to K_S^0, Λ, Ξ, and ϕ. The results are shown in Fig. 9 for the 60% most central events and also for the 0%–20% and 20%–60% centrality bins at midrapidity $|y| < 1$. Because of limited statistics, Ξ and ϕ
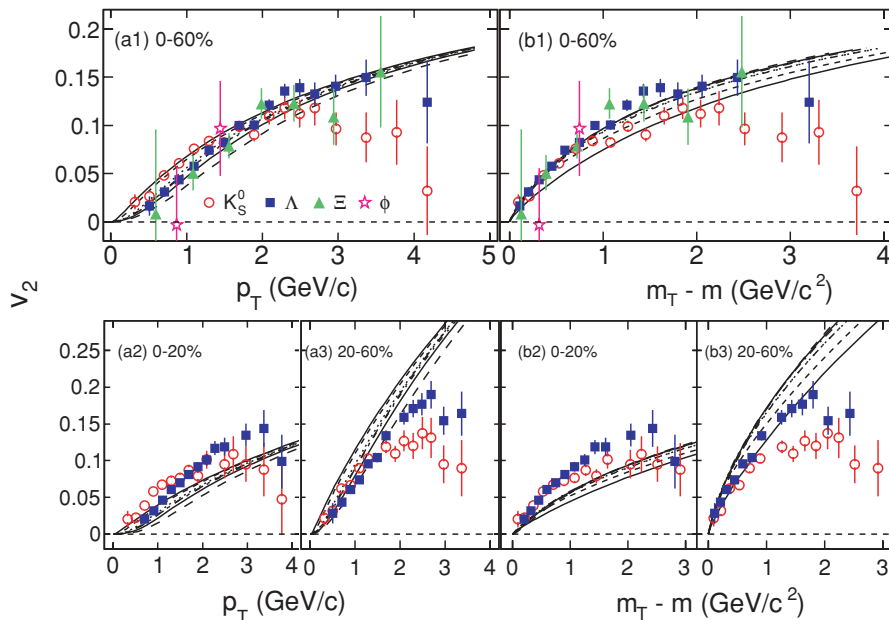

FIG. 9. (Color online) v_2 of K_S^0 (open circles), Λ (solid squares), Ξ (solid triangles), and ϕ (open stars) as a function of p_T for (a1) 0%–60%, (a2) 0%–20%, and (a3) 20%–60% and as a function of $m_T - m$ for (b1) 0%–60%, (b2) 0%–20%, and (b3) 20%–60%. For comparison, the results from ideal hydrodynamic calculations [49,50] are also shown. At a given p_T, from top to bottom, the curves represent π, K, p, ϕ, Λ, Ξ, and Ω. When p_T is converted to $m_T - m$, this mass hierarchy is reversed in the model results. All data are from $\sqrt{s_{NN}} = 200$ GeV Cu + Cu collisions. The error bars are shown only for the statistical uncertainties.
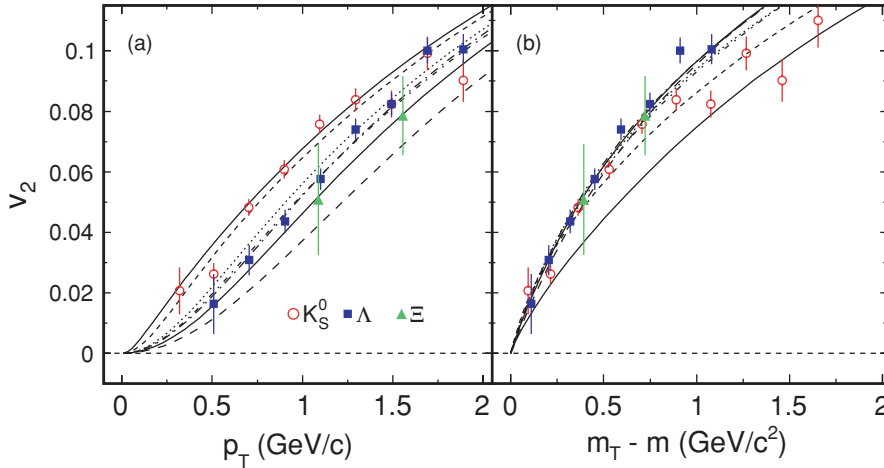
FIG. 10. (Color online) Same as Fig. 9(a1) and 9(b1), but expanded for the low p_T and $m_T - m$ regions. The data points with large errors have not been plotted. At a given p_T, from top to bottom, the curves represent the ideal hydrodynamic calculations for π, K, p, ϕ, Λ, Ξ, and Ω [49,50]. When p_T is converted to $m_T - m$, this mass hierarchy is reversed in the model results. All data are from 0% to 60% Cu + Cu collisions at $\sqrt{s_{NN}} = 200$ GeV. The error bars are shown only for the statistical uncertainties.

are only shown for the 0%–60% bin. The results from ideal hydrodynamic calculations [49,50] for each centrality bin are shown for π, K, p, ϕ, Λ, Ξ, and Ω, which are displayed by the curves from top (bottom) to bottom (top) for the p_T ($m_T - m$) dependence.

The gross features of p_T dependence and hadron-type dependence are similar to those observed in 200 GeV Au + Au collisions [31]. At low p_T, the hadron mass hierarchy [at a given p_T, the heavier the hadron, the smaller the $v_2(p_T)$] is reproduced by ideal hydrodynamic calculations. [See Fig. 10(a) for clarity.] Multiple-strange-quark hadrons Ξ and ϕ, which participate less in later hadronic interactions than do single-strange-quark hadrons K_S^0 and Λ, have sizable v_2. In particular, Ξ is consistent with the mass ordering shown in Fig. 9(a1). While the model can roughly reproduce the magnitude of the data for the 60% most central events sample, there is an obvious disagreement in centrality selected data. The model underpredicts $v_2(p_T)$ in the 0%–20% bin while it overpredicts the data in the 20%–60% bin. Effects not included in the model that may be relevant are geometrical fluctuations in the initial conditions and finite viscosity effects. It is unclear whether these effects can account for the difference between the model and the data.

At higher p_T, the hydrodynamic model mass ordering breaks. $v_2(p_T)$ appears to depend on hadron type: $v_2(p_T)$ is grouped by mesons and baryons, with magnitude depending on the number of quarks within the mesons or baryons. Over the entire p_T region, both the data and the model exhibit the same qualitative centrality dependence as observed for 200 GeV Au + Au collisions [31]: the more peripheral the collision, the larger the v_2 values. Compared to the results for 200 GeV Au + Au collisions [31], the splitting of K_S^0 and Λ $v_2(p_T)$ is smaller in both the mass ordering region and the hadron-type dependence region. This indicates smaller collective flow in Cu + Cu than Au + Au collisions, which will be seen more clearly in Sec. IV D.

The transverse kinetic energy scaling first observed in Au + Au collisions is also tested in Fig. 9. The results in Figs. 9 (a1)–9(a3) are replotted as a function of the transverse kinetic energy $m_T - m$ in Figs. 9 (b1)–9(b3). The quantity m denotes the rest mass of a given hadron. In the low $m_T - m$ region, $v_2(m_T - m)$ is a linearly increasing function and

independent of hadron mass. Transverse kinetic energy scaling holds in the region $m_T - m < 0.8$ GeV/c^2, as observed in Au + Au collisions [31,51]. Calculations using ideal hydrodynamics are shown in each panel as a function of $m_T - m$. Contrary to the mass ordering as a function of p_T, the model shows the reversed mass ordering as a function of $m_T - m$: the heavier the hadron, the larger the $v_2(m_T - m)$ value. The results of K_S^0, Λ, and Ξ exhibit $m_T - m$ scaling in each centrality bin, while the model does not show any scaling. Because no pion results are available, the scaling test of the data is not conclusive. All these effects can be seen more clearly in Fig. 10.

C. Quark-number scaling

In Au + Au collisions in the intermediate p_T region, $2 < p_T < 4$ GeV/c, the baryon-meson grouping of $v_2(p_T)$ follows the number-of-quark scaling: the v_2 of all hadrons fall onto a universal curve once v_2 and p_T are divided by the number of quarks, n_q, in a given hadron [31,52]. The observed scaling can be explained by the coalescence or recombination models [22,53,54], indicating the constituent quark degree of freedom has been manifested before hadronization takes place. n_q scaling is tested for various centrality bins in 200 GeV Cu + Cu collisions: $v_2(p_T)$ and $v_2(m_T - m)$ scaled by n_q are shown in Figs. 11(a1)–11(a3) and 11(b1)–11(b3), respectively. The n_q- scaling formula of Ref. [55], which can be written as

$$\frac{f_{v_2}(p_T)}{n_q} = \frac{a}{1 + e^{-(p_T/n_q - b)/c}} - d, \qquad (13)$$

has been fitted to the data both in p_T and $m_T - m$ for each centrality bin. In this formula, a, b, c, and d are fit parameters and n_q is the number of quarks. The n_q scaling is observed for $p_T/n_q > 0.8$ GeV/c, whereas it is seen for the entire $(m_T - m)/n_q$ region. Below $(m_T - m)/n_q \sim 0.4$ GeV/c^2, the $m_T - m$ scaling that was established at low p_T, now scaled by n_q, leads to the combined $(m_T - m)/n_q$ scaling. The universal n_q scaling of v_2 suggests the manifestation of early partonic dynamics in both Au + Au and Cu + Cu collisions.
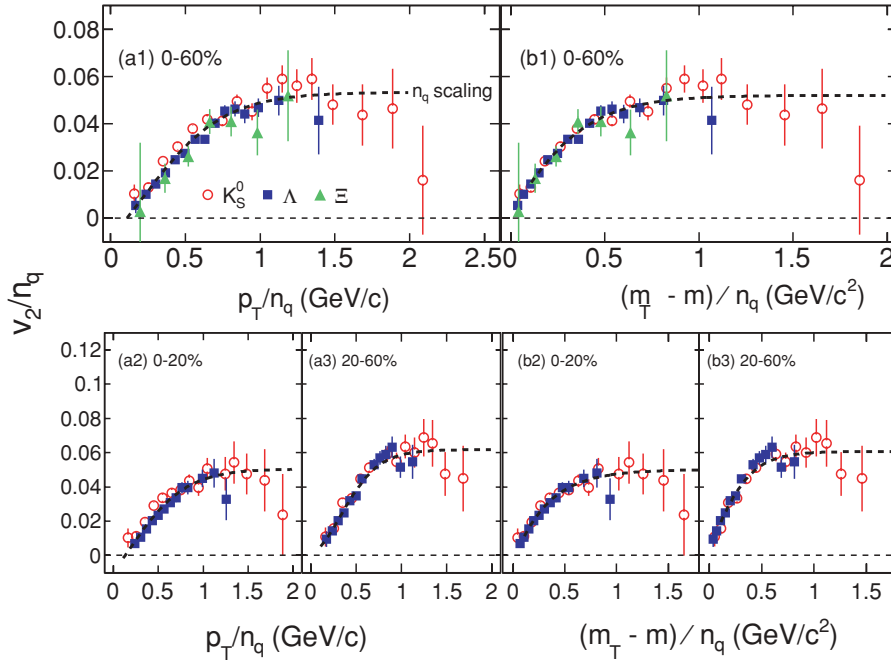
FIG. 11. (Color online) v_2/n_q versus p_T/n_q [panels (a1)–(a3)] and $(m_T - m)/n_q$ [panels (b1)–(b3)], where n_q is the number of constituent quarks in the hadron. The parametrization Eq. (13) fitted to the data is shown as the dashed curves. All data are from $\sqrt{s_{NN}} = 200$ GeV Cu + Cu collisions. The error bars are shown only for the statistical uncertainties.

D. Centrality and system-size dependence

The centrality and system-size dependence of v_2 is related to the physics of the system created in high-energy nuclear collisions. In the ideal hydrodynamic limit the centrality dependence of elliptic flow is mostly defined by the elliptic anisotropy of the overlapping region of the colliding nuclei, and in the low-density limit it is mostly defined by the product of the elliptic anisotropy and the multiplicity. Thus, the centrality and system-size dependence of elliptic flow should be a good indicator of the degree of equilibration reached in the reaction [28].

For a study of the centrality dependence of $v_2(p_T)$ in Cu + Cu collisions together with Au + Au collisions, we divide $v_2(p_T)$ by the initial spatial anisotropy, eccentricity, to remove this geometric effect. The participant eccentricity is the initial configuration space eccentricity of the participants, which is defined by [56]

$$\varepsilon_{\text{part}} = \frac{\sqrt{(\sigma_y^2 - \sigma_x^2) + 4(\sigma_{xy}^2)}}{\sigma_y^2 + \sigma_x^2}. \tag{14}$$

In this formula, $\sigma_x^2 = \langle x^2 \rangle - \langle x \rangle^2$, $\sigma_y^2 = \langle y^2 \rangle - \langle y \rangle^2$, and $\sigma_{xy} = \langle xy \rangle - \langle x \rangle \langle y \rangle$, with x, y being the position of the participating nucleons in the transverse plane. The root mean square of the participant eccentricity,

$$\varepsilon_{\text{part}}\{2\} = \sqrt{\langle \varepsilon_{\text{part}}^2 \rangle}, \tag{15}$$

is calculated from the Monte Carlo–Glauber model [29,57] and the color glass condensate (CGC) model [58–61]. (See Table II for $\varepsilon_{\text{part}}\{2\}$.) Because the FTPC event plane is constructed from the hadrons that have their origin in participant nucleons and the FTPC event plane resolution is less than 0.2, what we actually measure is the root mean square of v_2 with respect to the participant plane [62]. In this case, $\varepsilon_{\text{part}}\{2\}$ is the

appropriate measure of the initial geometric anisotropy taking the event-by-event fluctuations into account [62–64]. Figure 12 shows the centrality dependence of $v_2(p_T)/\varepsilon_{\text{part}}\{2\}$ for $h^{\pm}$ in 200 and 62.4 GeV Cu + Cu collisions. For a given centrality bin, $v_2(p_T)/\varepsilon_{\text{part}}\{2\}$ initially increases with p_T and then flattens or falls off at higher p_T. After the geometric effect is removed, the ordering of the distributions as a function of centrality, observed in Fig. 7, is reversed: the more central the collision, the higher the $v_2(p_T)/\varepsilon_{\text{part}}\{2\}$. This suggests that the strength of collective motion is larger in more central collisions.

To further study the centrality dependence of strange hadron v_2, we normalized the n_q scaled values by $\varepsilon_{\text{part}}\{2\}$ and plotted them as a function of $(m_T - m)/n_q$. The centrality dependence of K_S^0 and Λ results are shown in Fig. 13. The solid symbols

TABLE II. Participant eccentricity $\varepsilon_{\text{part}}\{2\}$ and number of participants N_{part} from the Monte Carlo–Glauber model [29,57] and color glass condensate (CGC) model [58–61] calculations in Au + Au and Cu + Cu collisions at $\sqrt{s_{NN}} = 200$ GeV. The quoted errors are total statistical and systematic uncertainties added in quadrature.

|	Centrality	$\varepsilon_{\text{part}}\{2\}$ (CGC)	$\varepsilon_{\text{part}}\{2\}$ (Glauber)	N_{part}
Au + Au	0%–80%	0.338 ± 0.002	0.302 ± 0.004	126 ± 8
	0%–10%	0.148 ± 0.001	0.123 ± 0.003	326 ± 6
	10%–40%	0.353 ± 0.001	0.296 ± 0.009	173 ± 10
	40%–80%	0.554 ± 0.002	0.533 ± 0.018	42 ± 7
Cu + Cu	0%–60%	0.336 ± 0.009	0.350 ± 0.008	51 ± 2
	0%–20%	0.230 ± 0.010	0.235 ± 0.008	87 ± 2
	20%–60%	0.434 ± 0.003	0.468 ± 0.016	34 ± 1
	0%–10%	0.187 ± 0.002	0.197 ± 0.002	99 ± 2
	10%–20%	0.281 ± 0.002	0.279 ± 0.008	75 ± 2
	20%–30%	0.360 ± 0.003	0.369 ± 0.009	54 ± 1
	30%–40%	0.428 ± 0.002	0.458 ± 0.017	38 ± 1
	40%–50%	0.490 ± 0.002	0.550 ± 0.021	26 ± 1
	50%–60%	0.555 ± 0.004	0.643 ± 0.031	17 ± 1
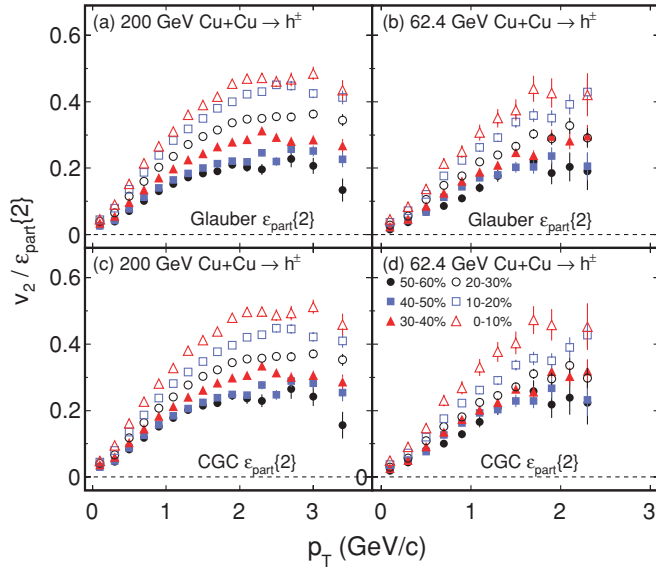
FIG. 12. (Color online) v_2 scaled by participant eccentricity as a function of p_T in $\sqrt{s_{NN}} = 200$ and 62.4 GeV Cu + Cu collisions. The error bars are shown only for the statistical uncertainties.

show from top to bottom the results from 0%–20% and 20%–60% centrality Cu + Cu collisions. For comparison, the results from 200 GeV Au + Au collisions [31] are shown by open symbols in Fig. 13. The results in Au + Au collisions are
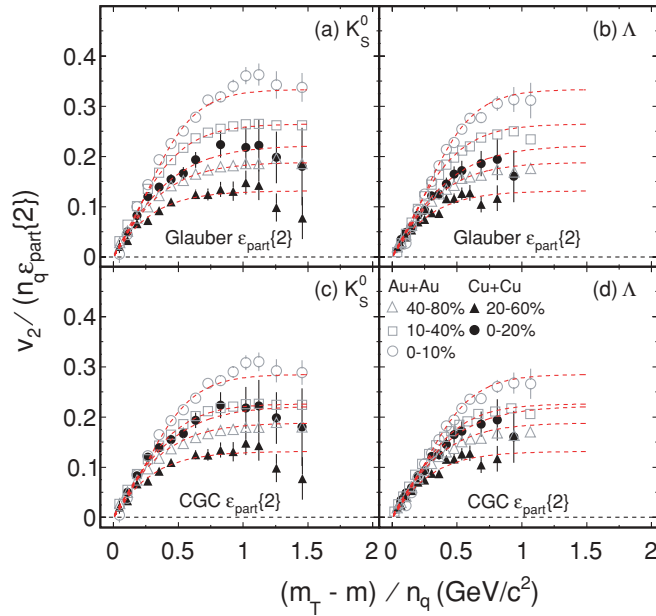

FIG. 13. (Color online) Centrality dependence of v_2 scaled by number of quarks and participant eccentricity $[v_2/(n_q \varepsilon_{\text{part}}\{2\})]$ for K_S^0 (left) and Λ (right) as a function of $(m_T - m)/n_q$ in 0%–10%, 10%–40%, and 40%–80% Au + Au collisions (open symbols) [31] and 0%–20% and 20%–60% Cu + Cu collisions (solid symbols) at $\sqrt{s_{NN}} = 200$ GeV. Curves are the results of n_q scaling fits from Eq. (13) normalized by $\varepsilon_{\text{part}}\{2\}$ to combined K_S^0 and Λ for five centrality bins. At a given p_T, from top to bottom, the curves show a decreasing trend as N_{part} decreases. The error bars are shown only for the statistical uncertainties.
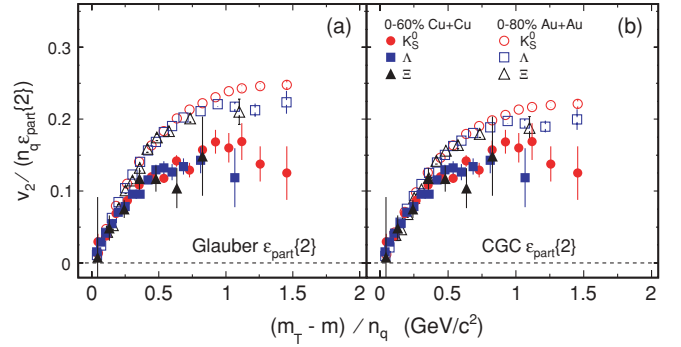

FIG. 14. (Color online) Number of quarks and participant eccentricity scaled v_2 $[v_2/(n_q \varepsilon_{\text{part}}\{2\})]$ of identified particles as a function of $(m_T - m)/n_q$ in 0%–80% Au + Au collisions (open symbols) [31] and 0%–60% Cu + Cu collisions (solid symbols) at $\sqrt{s_{NN}} = 200$ GeV. Circles, squares, and triangles represent the data for K_S^0, Λ, and Ξ, respectively. The error bars are shown only for the statistical uncertainties.

slightly different ($\sim$10% larger) from the previous published results [31], which were calculated directly from the wide centrality bins. From top to bottom, the results are from 0%–10%, 10%–40%, and 40%–80% centrality bins. For clarity, K_S^0 and Λ results are shown in different panels. Curves represent n_q scaling fits from Eq. (13) normalized by $\varepsilon_{\text{part}}\{2\}$ to the combined data of K_S^0 and Λ for five centrality bins. For a given centrality, K_S^0 and Λ results follow a universal curve, which means partonic collective flow is explicitly seen in the measured scaling with n_q and $\varepsilon_{\text{part}}\{2\}$. For a given collision system, the stronger partonic collective flow is apparent as higher scaled v_2 values in more central collisions. To study the system-size dependence of the scaling properties, the results from 0% to 60% centrality Cu + Cu and 0% to 80% Au + Au collisions are shown in Fig. 14. The stronger collective motion in Au + Au collisions compared to that in Cu + Cu collisions becomes obvious, although the constituent quark degrees of freedom have been taken into account in both systems.

In the ideal hydrodynamic limit where dynamic thermalization is reached, the mean free path is much less than the geometric size of the system. The geometric size of the system and the centrality dependence of flow is totally governed by the initial geometry (eccentricity) [28]. Because there is no universal scaling with the eccentricity among either different collision centralities or different collision system sizes, this indicates that the ideal hydrodynamic limit is not reached in Cu + Cu collisions, presumably because the assumption of thermalization is not attained. In addition, $v_2/(n_q \varepsilon_{\text{part}}\{2\})$ shows an increasing trend as a function of N_{part} (see Fig. 13). Table II lists the values of eccentricity and N_{part} for the used centrality bins in Au + Au and Cu + Cu collisions. This suggests that the measured v_2 is not only dependent on the initial geometry but also on N_{part}.

Theoretical analyses found that the centrality and system-size dependence of v_2 can be described by a simple model based on eccentricity scaling and incomplete thermalization. Within these models the lack of perfect equilibration allows for estimates of the effective parton cross section in the quark-gluon plasma and of the shear viscosity to entropy density ratio

(η/s) [33,65]. Thus, the v_2 results from Cu + Cu collisions reported in this article should allow extraction of η/s and extrapolation to the ideal hydrodynamic limit.

V. SUMMARY

We present STAR results on midrapidity elliptic flow v_2 for charged hadrons $h^{\pm}$ and strangeness-containing hadrons K_S^0, Λ, Ξ, and ϕ from Cu + Cu collisions at $\sqrt{s_{NN}} = 62.4$ and 200 GeV at RHIC. The centrality dependence of v_2 for different system sizes as a function of the transverse momentum p_T is presented. To estimate the systematic uncertainties, we studied various measurement methods. Below $p_T \sim$ 4GeV/c, nonflow correlations are reduced with the event plane constructed from hadrons produced in the forward regions $(2.5 < |\eta| < 4.0)$. We obtained an estimate of the systematic uncertainties due to the remaining nonflow contributions based on correlations measured in $p + p$ collisions.

For a given centrality bin, p_T and hadron-type dependencies of strange hadron v_2 are similar to those found in Au + Au collisions [31]: (i) In the low p_T region, $p_T < 2$ GeV/c, the hadron mass hierarchy is observed as expected in ideal hydrodynamic calculations: at fixed p_T, the larger the hadron mass, the smaller the v_2. (ii) In the intermediate p_T region, $2 < p_T < 4$ GeV/c, v_2 as a function of either p_T or $m_T - m$ follows a scaling with the number of constituent quarks

n_q. Larger $v_2/(n_q \varepsilon_{\mathrm{part}}\{2\})$ values are seen in more central collisions, indicating stronger collective flow developed in more central collisions. The comparison with Au + Au collisions that go further in density shows eccentricity scaled v_2 values depend on the system size (N_{part}). This suggests that the ideal hydrodynamic limit is not reached in Cu + Cu collisions, presumably because the assumption of thermalization is not attained.

[1] S. A. Voloshin and Y. Zhang, Z. Phys. C **70**, 665 (1996).
[2] A. M. Poskanzer and S. A. Voloshin, Phys. Rev. C **58**, 1671 (1998).
[3] S. A. Voloshin, A. M. Poskanzer, and R. Snellings, arXiv:0809.2949 [nucl-ex].
[4] Y. Lu, M. Bleicher, F. Liu, Z. Liu, H. Petersen, P. Soresen, H. Stöcker, N. Xu, and X. Zhu, J. Phys. G **32**, 1121 (2006).
[5] H. Sorge, Phys. Rev. Lett. **78**, 2309 (1997).
[6] H. Sorge, Phys. Lett. B **402**, 251 (1997); Phys. Rev. Lett. **82**, 2048 (1999).
[7] J.-Y. Ollitrault, Phys. Rev. D **46**, 229 (1992).
[8] D. Teaney, J. Lauret, and E. V. Shuryak, Phys. Rev. Lett. **86**, 4783 (2001).
[9] J. Adams *et al.* (STAR Collaboration), Nucl. Phys. A **757**, 102 (2005).
[10] K. Adcox *et al.* (PHENIX Collaboration), Nucl. Phys. A **757**, 184 (2005).
[11] C. Adler *et al.* (STAR Collaboration), Phys. Rev. Lett. **87**, 182301 (2001).
[12] J. Adams *et al.* (STAR Collaboration), Phys. Rev. Lett. **92**, 052302 (2004).
[13] J. Adams *et al.* (STAR Collaboration), Phys. Rev. Lett. **95**, 122301 (2005).
[14] A. Shor, Phys. Rev. Lett. **54**, 1122 (1985).
[15] H. van Hecke, H. Sorge, and N. Xu, Phys. Rev. Lett. **81**, 5764 (1998).
[16] S. A. Bass, A. Dumitru, M. Bleicher, L. Bravina, E. Zabrodin, H. Stocker, and W. Greiner, Phys. Rev. C **60**, 021902(R) (1999);

A. Dumitru, S. A. Bass, M. Bleicher, H. Stocker, and W. Greiner, Phys. Lett. B **460**, 411 (1999); S. A. Bass and A. Dumitru, Phys. Rev. C **61**, 064909 (2000).
[17] Y. Cheng, F. Liu, Z. Liu, K. Schweda, and N. Xu, Phys. Rev. C **68**, 034910 (2003).
[18] S. F. Biagi *et al.*, Nucl. Phys. B **186**, 1 (1981).
[19] R. A. Muller, Phys. Lett. B **38**, 123 (1972).
[20] B. I. Abelev *et al.* (STAR Collaboration), Phys. Rev. Lett. **99**, 112301 (2007).
[21] S. Afanasiev *et al.* (PHENIX Collaboration), Phys. Rev. Lett. **99**, 052301 (2007).
[22] D. Molnar and S. A. Voloshin, Phys. Rev. Lett. **91**, 092301 (2003).
[23] K. H. Ackermann *et al.* (STAR Collaboration), Phys. Rev. Lett. **86**, 402 (2001).
[24] P. F. Kolb, J. Sollfrank, and U. Heinz, Phys. Rev. C **62**, 054909 (2000).
[25] P. Kolb, J. Sollfrank, and U. Heinz, Phys. Lett. B **459**, 667 (1999).
[26] D. Teaney and E. V. Shuryak, Phys. Rev. Lett. **83**, 4951 (1999).
[27] T. D. Lee, Nucl. Phys. A **750**, 1 (2005).
[28] S. A. Voloshin and A. M. Poskanzer, Phys. Lett. B **474**, 27 (2000).
[29] M. Miller and R. Snellings, arXiv:nucl-ex/0312008.
[30] C. Adler *et al.* (STAR Collaboration), Phys. Rev. C **66**, 034904 (2002).
[31] B. I. Abelev *et al.* (STAR Collaboration), Phys. Rev. C **77**, 054901 (2008).
[32] H. Heiselberg and A. M. Levy, Phys. Rev. C **59**, 2716 (1999).

[33] H. J. Drescher, A. Dumitru, C. Gombeaud, and J. Y. Ollitrault, Phys. Rev. C **76**, 024905 (2007).

[34] STAR Collaboration (in preparation).

[35] K. H. Ackermann *et al.* (STAR Collaboration), Nucl. Instrum. Methods A **499**, 624 (2003).

[36] K. H. Ackermann *et al.* (STAR Collaboration), Nucl. Instrum. Methods A **499**, 713 (2003).

[37] C. Adler *et al.* (STAR Collaboration), Phys. Rev. Lett. **89**, 202301 (2002).

[38] J. Adams *et al.*, Phys. Lett. B **612**, 181 (2005); C. Adler *et al.*, Phys. Rev. C **65**, 041901(R) (2002).

[39] J. Barrette *et al.* (E877 Collaboration), Phys. Rev. C **56**, 3254 (1997).

[40] J. Adams *et al.* (STAR Collaboration), Phys. Rev. C **72**, 014904 (2005).

[41] I. Selyuzhenkov and S. Voloshin, Phys. Rev. C **77**, 034904 (2008).

[42] N. Borghini and J. Y. Ollitrault, Phys. Rev. C **70**, 064905 (2004).

[43] J. Adams *et al.* (STAR Collaboration), Phys. Rev. Lett. **93**, 252301 (2004).

[44] C. Adler *et al.* (STAR Collaboration), Phys. Rev. Lett. **90**, 082302 (2003).

[45] L. Molnar (STAR Collaboration), J. Phys. G **34**, S593 (2006).

[46] B. Alver *et al.* (PHOBOS Collaboration), Phys. Rev. Lett. **104**, 062301 (2010).

[47] B. I. Abelev *et al.* (STAR Collaboration), arXiv:0912.3977.

[48] Y. Bai (STAR Collaboration), in Proceedings of Strange Quark Matter 2008, 2008.

[49] P. Huovinen and P. V. Ruuskanen, Annu. Rev. Nucl. Part. Sci. **56**, 163 (2006).

[50] P. Huovinen (private communication).

[51] A. Adare *et al.* (PHENIX Collaboration), Phys. Rev. Lett. **98**, 162301 (2007); A. Taranenko, J. Phys. G **34**, S1069 (2007).

[52] B. I. Abelev *et al.* (STAR Collaboration), Phys. Rev. C **75**, 054906 (2007).

[53] R. J. Fries, B. Müller, C. Nonaka, and S. A. Bass, Phys. Rev. Lett. **90**, 202303 (2003).

[54] R. C. Hwa and C. B. Yang, Phys. Rev. C **67**, 064902 (2003).

[55] X. Dong, S. Esumi, P. Sorensen, N. Xu, and Z. Xu, Phys. Lett. B **597**, 328 (2004).

[56] B. Alver *et al.* (PHOBOS Collaboration), Phys. Rev. Lett. **98**, 242302 (2007).

[57] M. L. Miller, K. Reygers, S. J. Sanders, and P. Steinberg, Annu. Rev. Nucl. Part. Sci. **57**, 205 (2007).

[58] A. Adil, H. J. Drescher, A. Dumitru, A. Hayashigaki, and Y. Nara, Phys. Rev. C **74**, 044905 (2006).

[59] H. J. Drescher and Y. Nara, Phys. Rev. C **75**, 034905 (2007).

[60] H. J. Drescher and Y. Nara, Phys. Rev. C **76**, 041903(R) (2007).

[61] T. Hirano and Y. Nara, Phys. Rev. C **79**, 064904 (2009).

[62] J. Y. Ollitrault, A. M. Poskanzer, and S. A. Voloshin, Phys. Rev. C **80**, 014904 (2009).

[63] S. Voloshin, arXiv:nucl-th/0606022.

[64] B. Alver *et al.* (PHOBOS Collaboration), Phys. Rev. C **77**, 014906 (2008).

[65] C. Gombeaud and J. Y. Ollitrault, Phys. Rev. C **77**, 054904 (2008).